Check for updates

View Article Online
View Journal

Journal of
Materials Chemistry A

Materials for energy and sustainability

Accepted Manuscript

This article can be cited before page numbers have been issued, to do this please use: M. Li, F. Hernandez Baena, S. Matsuo, M. Chen, B. Izelaar, R. Kortlever and A. Urakawa, *J. Mater. Chem. A*, 2026, DOI: 10.1039/D5TA09769J.

This is an Accepted Manuscript, which has been through the Royal Society of Chemistry peer review process and has been accepted for publication.

Accepted Manuscripts are published online shortly after acceptance, before technical editing, formatting and proof reading. Using this free service, authors can make their results available to the community, in citable form, before we publish the edited article. We will replace this Accepted Manuscript with the edited and formatted Advance Article as soon as it is available.

You can find more information about Accepted Manuscripts in the Information for Authors.

Please note that technical editing may introduce minor changes to the text and/or graphics, which may alter content. The journal's standard Terms & Conditions and the Ethical guidelines still apply. In no event shall the Royal Society of Chemistry be held responsible for any errors or omissions in this Accepted Manuscript or any consequences arising from the use of any information it contains.

ROYAL SOCIETY OF CHEMISTRY

rsc.li/materials-a

View Article Online
DOI: 10.1039/D5TA09769J

ARTICLE

Tuning Product Selectivity in Direct Electroreduction of NO *via* Phase Engineering of MoS_2 Nanosheets in Water-fed PEM Electrolyzer

Received 00th January 20xx,
Accepted 00th January 20xx

DOI: 10.1039/x0xx00000x

Min Li,[a,c] Frank Hernandez Baena,[a] Shota Matsuo,[a] Mingliang Chen,[a] Boaz Izelaar,[b,c] Ruud Kortlever,[b,c] Atsushi Urakawa*[a, c]

Electrochemical conversion of NO from gaseous pollutants into ammonia using abundant and cost-effective catalyst materials holds great promise for pollutant abatement and for advancing a more closed, sustainable nitrogen cycle. However, regulating product selectivity remains challenging because NO reduction involves complex multielectron/proton pathways. Here, we report two different crystal phases MoS_2 (2H and 1T') exhibiting prominent activity in the electrochemical NO reduction reaction (NORR), but showing different selectivity. The faradaic efficiency of ammonia reaches 86% over 2H-MoS_2, outperforming 1T'-MoS_2 (31%) at 2.1 V. In contrast, 1T'-MoS_2 displays higher selectivity towards N_2, especially at lower cell voltage (50% at 1.7 V). Kinetic and spectroscopic analyses further suggest phase-dependent rate-control characteristics, consistent with distinct pathway preferences on 1T' versus 2H. Overall, these results demonstrate that NORR activity and selectivity can be efficiently tuned by choosing the appropriate MoS_2 phase, providing a simple strategy to tune product selectivity in complex multistep reactions.

Introduction

Nitrogen, the fifth most abundant element on earth, plays an essential role as macronutrient for all living organisms.[1] Within the global nitrogen cycle, various inorganic nitrogenous compounds, including ammonia (NH_3), hydroxylamine (NH_2OH), hydrazine (N_2H_4), nitrous oxide (N_2O), nitric oxide (NO), nitrogen dioxide (NO_2), nitrite (NO_2^-), and nitrate (NO_3^-) are produced in significant quantities by industrial chemical processes.[2] Many of these species, notably NO_x (NO, NO_2 and N_2O) are prominent environmental pollutants. Consequently, mitigating NO_x emissions from fossil fuel combustion, such as power plants and automotive engines, represents a critical focus within nitrogen chemistry.[3] Among these pollutants, NO typically constitutes approximately 95% of NO_x in flue gas.[4]

Conventional selective catalytic reduction (SCR) methods effectively convert NO into harmless dinitrogen gas (N_2).[5] However, SCR requires the input of reducing agents such as NH_3 or H_2, imposing additional energy and material demands.[6] NH_3 itself holds significant importance in agriculture and has recently emerged as a potential H_2 energy carrier.[7, 8] Its industrial production is primarily achieved through the Haber-Bosch process, a thermochemically intensive reaction that operates under high pressure (150-300 bar) and temperature (400–500 °C). This process accounts for approximately 1-2% of global energy consumption and 1-1.5% of global CO_2 emissions annually.[9]

Thus, electrochemical approaches for the NO reduction reaction (NORR) offer a promising alternative for both NO abatement and NH_3 synthesis, thereby contributing to a more sustainable nitrogen cycle.[10, 11] In particular, the NORR presents thermodynamic advantages: the standard reduction potential of NO to NH_3 (0.71 V vs. RHE) is significantly more positive than that of the nitrogen reduction reaction (NRR, 0.093 V vs. RHE)[12] and hydrogen evolution reaction (HER), theoretically implying a more favourable reaction path.[13, 14] Nonetheless, the practical implementation of the NORR has been hindered by the low solubility of NO in aqueous media (1.92 $mmol \cdot L^{-1} \cdot atm^{-1}$ at 25 °C), which limits its availability at the electrode surface.[15] Therefore, utilizing membrane electrode assembly (MEA) configurations, more specifically in a proton exchange membrane (PEM) electrolyzer allows direct gaseous NORR, which improves control over reaction environment and reduces internal resistance. Beyond traditional H-cell configuration, a PEM electrolyzer facilitates more controlled reagent flow and reaction kinetics, making it attractive for future electrochemical NO conversion technologies **(Figure S1)**.[16, 17]

To date, significant advances have been made in the development of catalytic materials for the NORR, including pure transition metals (TMs)[18] noble metals[19], alloys[20], metal oxides[21] and single-atom catalysts (SACs)[22]. Nonetheless, challenges still remain due to the low abundance and thus high costs associated with noble metals, the limited activity of pure

[a] Department of Chemical Engineering, Delft University of Technology, Van der Maasweg 9, 2629 HZ, Delft, the Netherlands
[b] Department of Process & Energy, Delft University of Technology, Leeghwaterstraat 39, 2628 CB, Delft, the Netherlands
[c] e-Refinery Institute, Delft University of Technology, Leeghwaterstraat 39, 2628 CB Delft, the Netherlands
Supplementary Information available. See DOI: 10.1039/x0xx00000x

Open Access Article. Published on 14 April 2026. Downloaded on 21/4/2026 3:58:20 PM.
This article is licensed under a Creative Commons Attribution 3.0 Unported Licence.

Journal of Materials Chemistry A Accepted Manuscript

View Article Online
DOI: 10.1039/D5TA09769J

Open Access Article. Published on 14 April 2026. Downloaded on 21/4/2026 3:58:20 PM.
This article is licensed under a Creative Commons Attribution 3.0 Unported Licence.

TMs, and the insufficient long-term stability of SACs, emphasizing the need to design cost-effective, efficient, and durable electrocatalysts for denitrification.[23] Among transition metal dichalcogenides (TMDs), monolayer molybdenum disulfide (MoS_2) stands out as an abundant, low-cost, and versatile electrocatalyst, having already demonstrated excellent HER.[24] Compared to the commonly studied semiconducting 2H phase, MoS_2 in its octahedral (1T) or distorted octahedral (1T') configurations has shown superior catalytic activity for the HER.[25] A key advantage of TMDs is the tunability of their atomic-scale structure, which offers opportunities to adjust the selectivity of multielectron/proton reactions.[26] In this context, exploring phase-dependent electrocatalytic activity is vital to achieve a deeper understanding of the origins of catalytic performance. Nakamura *et al.*[27] identified a Mo(V) intermediate unique to 1T-MoS_2 that promotes N-N coupling selectivity by decoupling proton and electron transfer to sequential proton-electron transfer (SPET) pathway. In contrast, 2H-MoS_2 favours NH_3 production during NO_3^- reduction via concerted proton-electron transfer (CPET) pathway. Similarly, Yu *et al.*[28] investigated the reaction at near-neutral pH, reporting that the strong hydrogen affinity and favourable hydrogenation of nitrogenous intermediates on 1T-MoS_2 make this phase particularly promising for NO_3^- to NH_3 conversion. However, these studies have primarily focused on liquid-phase nitrate reduction under mild pH conditions (pH 4-7) in three-electrode cell configurations. Therefore, the role of MoS_2 crystal phases in the direct gas-phase NO reduction under acidic conditions in industrially relevant PEM electrolyzers remains insufficiently understood and requires further investigation.

In this work, we explored phase-engineered MoS_2 nanosheets (2H and 1T') as effective catalysts for direct gaseous NO electroreduction in a PEM electrolyzer, enabling a pronounced and controllable selectivity switch between NH_3 and N_2. The 2H-MoS_2 achieved a high NH_3 yield of 558 $\mu mol \cdot cm^{-2} \cdot h^{-1}$ at 2.3 V and a highest FE of 86% at 2.1 V, exceeding the performance of the 1T' phase. Notably, the 1T' phase-dominant MoS_2 demonstrated greater selectivity for N-N coupling products (N_2), particularly under low applied potentials, 50% FE towards N_2 at 1.7V. To uncover the origin of this phase-dependent selectivity, we establish a mechanistic picture by integrating LSV with local Tafel/derivative analysis, an apparent kinetic isotope effect, and *ex situ* NO-DRIFTS, revealing distinct apparent rate-control characteristics on 2H versus 1T', thus we connect the stronger NO-derived adsorption signatures o 1T' to coverage-enabled N-N coupling, whereas the pronounced apparent KIE on 2H supports a proton-coupled hydrogenation contribution consistent with enhanced NH_3 selectivity. Overall, these findings highlight phase engineering of TMDs catalysts as a practical strategy to tune product selectivity in complex multistep proton-electron transfer reactions.

Results and discussion

Material Synthesis and Characterizations

2H-MoS_2 (trigonal phase) material was successfully synthesized using a one-step hydrothermal method as illustrated in **Figure S2(a)**.[29] Meanwhile, distorted 1T'-MoS_2 (octahedral phase) was obtained by adding hydrazine monohydrate ($N_2H_4 \cdot H_2O$) during the synthesis, as depicted schematically in **Figure S2(b)**.[29] XRD patterns of the as-prepared samples are shown in **Figure 1(a)**. For the synthesized 2H-MoS_2, the (002) peak located at 13.9° shifted slightly towards lower angle compared to that of 14.4° in highly crystalline 2H-MoS_2 (JCPDS Card no. 73-1508). This was ascribed to the interlayer stress as a result of disordered structures.[30] The calculated interlayer distance of the synthesized 2H-MoS_2 is 0.62 nm, originating from the interference among the 2H-MoS_2 layers along the c-axis. At higher angles, the appearance of (100) and (110) peaks in 2H-MoS_2 sample (hereafter referred to as 2H-MoS_2) indicated the same basal plane orientation with highly crystalline 2H-MoS_2. For the synthesized 1T'-MoS_2 sample (hereafter referred to as 1T'-MoS_2), the (002) peak is drastically shifted to 9.2° compared to that peak of 2H-MoS_2, which indicates that the lattice expansion as the interlayers are intercalated with N_2H_4[31]. According to the Bragg equation, the corresponding interlayer distances of the peaks were 0.93 nm and 0.49 nm at 9.2° and 18.2°, respectively[32]. The broad XRD diffraction peak can be an indication of the coexistence of both 2H and 1T' phases in the hydrazine intercalated 1T' sample[33]. Scanning electron microscopy (SEM) images of the prepared 2H and 1T' MoS_2 samples were shown in **Figure 1(b & c)**. Both pictures show nano-flowers consisting of small, intersecting nanosheets. This morphology is characterized by short lateral dimensions and a lack of extended stacking, which geometrically necessitates a high density of exposed edge S atoms which are the active sites, compared to flat for bulk 2H-MoS_2. The disordered arrangement of these nanosheets prevents the Van der Waals restacking typical bulk crystals, thereby maximizing the accessible surface area and defect density.[34]

Figure 1(d) presents Raman spectra of the synthesized 2H and 1T' phase MoS_2 nanoflowers. The E^1_{2g} peak at 378 cm^{-1} and the A_{1g} one at 404 cm^{-1} show the opposite vibration of two S atoms with respect to the Mo atom and the out of plane opposite vibration of the S atoms in opposite directions, respectively. Compared to the 2H phase, 1T'-MoS_2 displays a slightly weaker E^1_{2g} band due to the existence of defects. Notably, there is no A_{1g} band presented in 1T' phase MoS_2 which indicates the weakened interactions between the adjacent layers because of the intercalated molecules to the MoS_2 layers(**Figure 1(a)**).[32]

Journal of Materials Chemistry A Accepted Manuscript

This journal is © The Royal Society of Chemistry 20xx

Please do not adjust margins

View Article Online
DOI: 10.1039/D5TA09769J

ARTICLE

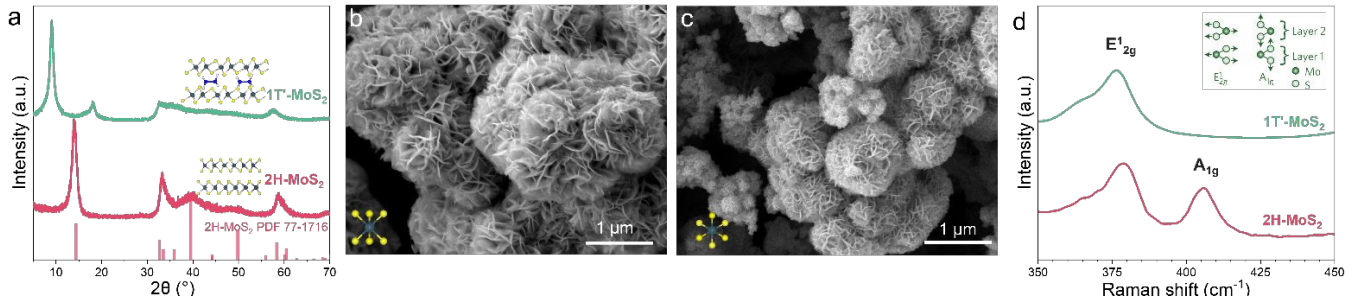

Figure 1. (a) XRD patterns of 2H- and 1T'-MoS_2; (b) & (c) SEM images of 2H- and 1T'-MoS_2; (d) Raman spectrum of 2H- and 1T'-MoS_2.

To better understand the electronic structure of as-prepared 2H- and 1T'-MoS_2, X-ray absorption near edge structure (XANES) spectroscopy was performed. Commercial 2H-MoS_2 was taken as the standard. The results (**Figure 2(a)**) suggest that the oxidation state of Mo in both samples is +4 as the energy positions of Mo K-edge are close to that of the commercial MoS_2 standard. However, the chemical state of Mo in 1T'-MoS_2 was a little lower than that of 2H-MoS_2 according to the spectra, which indicated the surface of 1T'-MoS_2 is electron rich. The valence state and near-surface composition of 2H and 1T' phases were further identified by X-ray photoelectron spectroscopy (XPS). All the spectrums are calibrated using C 1s peak at 284.8 eV. The energy shifts of the Mo (3d) and the S (2p) peaks further indicate the different electronic states of the 1T' and 2H phases.[35] As shown in **Figure 2(c)**, two peaks of Mo^{4+} (3d) at around 229 and 232 eV correspond to binding energies of Mo^{4+} $3d_{5/2}$ and $3d_{3/2}$ electrons in 2H-MoS_2, respectively. In addition to these two peaks, a new doublet peak (228.4 and 231.6 eV) appeared for 1T'-MoS_2[36]. The Mo ($3d_{5/2}$) peak of the 1T' phase shifted to a lower binding energy (0.88 eV) relative to that of the 2H-MoS_2, showing the increasing electron density on 1T'-MoS_2, which is consistent with the XANES studies. By deconvoluting the Mo (3d) peak, it can be estimated that 80% of Mo is in the 1T' phase in the as-prepared 1T'-MoS_2 samples. The S ($2p_{3/2}$) peak also showed a similar shift as Mo ($3d_{5/2}$) (**Figure 2(c)**). Compared to the 2H phase with one S (2p) doublet with the binding energy of 162.6 eV, the hydrazine-intercalated 1T' phase has an extra split S (2p) doublet peak at 161.3 eV. In addition, the XPS spectra of N (1s) is presented in **Figure S3**. The peak at 399.4 eV can be ascribed to the characteristic signals of intercalated or adsorbed N_2H_4 species[37], suggesting the occurrence of charge transfer from N to MoS_2. Importantly, the presence of N as an *n*-type dopant in MoS_2 can shift the Fermi level closer to the valence band, thereby facilitating charge transfer. This effect arises from band bending induced by the formation of Mo-N covalent bonds and the preferential removal of S atoms.[38, 39] Besides, the XPS analysis based on the survey scan indicates that the atomic ratio of Mo to S atoms is approximately 1:1.86 for 2H-MoS_2 but decreased to 1:1.63 for 1T'-MoS_2, indicating an increased number of S vacancies in the 1T' phase. (**Figure S4 & Table S1**).

Furthermore, the atomic coordination was investigated by extended X-ray absorption fine structure (EXAFS) spectroscopy. As shown in **Figure S5**, the Mo K-edge oscillation curve of 1T'-MoS_2 differs significantly from those of 2H-MoS_2 and commercial MoS_2, indicating substantial changes in local atomic arrangements. These differences are further clarified by the Fourier Transform (FT) profiles in real space (**Figure 2(b)**). For 2H-MoS_2, the FT curve features two main peaks at 1.96 Å and 2.85 Å, corresponding to the nearest Mo-S and Mo-Mo distances, respectively. In contrast, 1T'-MoS_2 exhibits a noticeable second peak at 2.48 Å instead of 2.85 Å in 2H-MoS_2, indicating a change in the Mo-Mo distance and the local structure changes. Additionally, the peak intensity of the Mo–S bond decreases for 1T'-MoS_2, likely due to defect formation induced by N_2H_4 intercalation, while the Mo-Mo peak intensity also decreased, suggesting a corresponding reduction in coordination number. These observations may indicate a structural transformation in which one sulfur basal plane of 1T-MoS_2 rotates by 60° along the c-axis relative to the 2H-phase trigonal prismatic structure, resulting in a distorted octahedral coordination (1T') (**Figure S6**).[40] To obtain quantitative structural parameters, EXAFS fitting was conducted in ARTEMIS[41] software, with results summarized in **Table S2 and Figure S7**.

Open Access Article. Published on 14 April 2026. Downloaded on 21/4/2026 3:58:20 PM.
This article is licensed under a Creative Commons Attribution 3.0 Unported Licence.

Journal of Materials Chemistry A Accepted Manuscript

View Article Online
DOI: 10.1039/C5TA09769J

Open Access Article. Published on 14 April 2026. Downloaded on 21/4/2026 3:58:20 PM.
This article is licensed under a Creative Commons Attribution 3.0 Unported Licence.

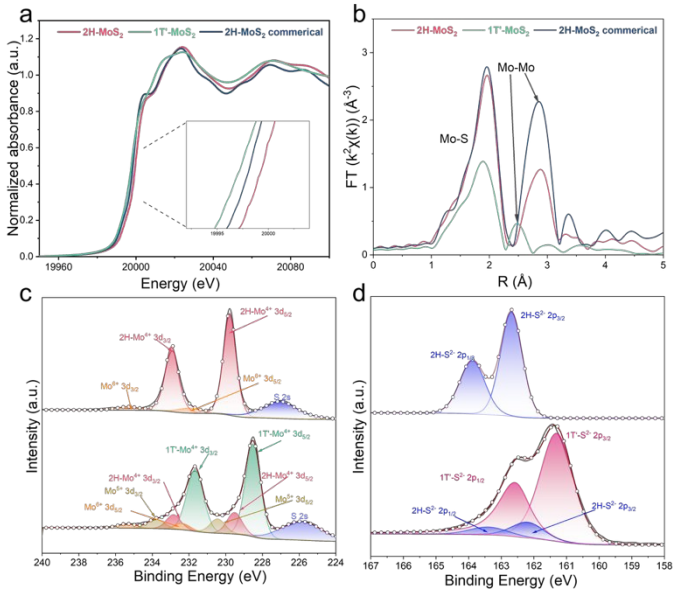

Figure 2. (a) XANES spectra & (b) k^2-weighted Fourier transformed EXAFS spectra of the Mo K-edge of the as-prepared and standard MoS_2 samples; (c) Mo 3d XPS spectra & (d) S 2p XPS spectra of as prepared 2H- and 1T'-MoS_2.

Optimal carbon ratio for electrocatalytic NORR

Prior to the evaluation of the MoS_2 catalysts for NORR in PEM electrolyzer, the optimal ratio of mixing as-synthesized MoS_2 materials with electrically conducting carbon black was first investigated. Conductive carbon black is indispensable to drop-casted electrodes for ensuring smooth charge transfer at the catalyst interface and maximizing the utilization of the catalyst surface, especially for MoS_2 given its intrinsic semiconducting nature. The tests were first performed in a rotating disk electrode (RDE) setup, which allows for more precise control of mass transport, speeding up the investigation process compared to multi-steps preparation for testing in PEM electrolyzer.[42] 2H-MoS_2 was used for this investigation, and the iR-corrected polarization curves in 0.1 M H_2SO_4 were used to compare performance with different relative carbon amounts. In the MoS_2/C (carbon black) composition, the loading of 2H-MoS_2 (1 mg·cm^{-2}) was kept constant and the amount of carbon black was changed with respect to the total weight of 2H-MoS_2 from 100 wt.% to 30 wt.%, decreasing with the step of 10 wt.%. The physically mixed 2H-MoS_2/C was drop-casted on a glassy carbon electrode in the RDE setup (see the method section for detailed description). The results are shown in **Figure S8**, 50 wt.% of Vulcan carbon black mixture exhibited the best electrochemical activity among all the mixing ratios, while a further increase in the amount of carbon black resulted in decreasing activity. Pure MoS_2 exhibited activity, but the performance was poor and lower than all the samples with carbon black mixing. Also, the electrochemical surface area (ECSA) was investigated by measuring the double-layer capacitance (C_{dL}) in the non-faradaic region. The results are shown in **Figure S9**. Derived from cyclic voltammetry (CV) curves obtained at various scan rates, the C_{dL} value was the highest at 50 wt.% carbon black mixture with 7.7 mF·cm^{-2} and decreased with higher amount carbon black (**Figure S10**).

The results from the RDE study suggest that a physical mixture of 50 wt.% of carbon black would perform best, therefore, pure MoS_2, 40, 50 and 60 wt.% of MoS_2 on carbon black were selected to test for NORR in PEM electrolyzer. To better understand the relationship between the mass transfer limitation and reaction activity under relative low concentration NO (5 vol% in He), different types of gas diffusion layers, namely hydrophilic Ti GDL and hydrophobic carbon paper (Sargent 39BB), were investigated. **Figure 3(a)** shows the FE towards different products during NORR for (i) pure MoS_2 with Ti GDL, (ii) pure MoS_2, (iii) 40, (iv) 50 and (v) 60 wt.% on carbon black with carbon paper (CP, for (ii)-(v)) at 2.1 V, respectively. The FE of the full tested cell potential range (from 1.7-2.3 V) is shown in **Figure S11**. Electrochemical NORR activity of only carbon black was also examined as a control experiment. Carbon black itself exhibits low total current density, intriguingly with a reasonable selectivity towards ammonia (**Figure S12**).

Mainly H_2 was produced when using a Ti GDL, due to its hydrophilic character. A thin water layer could possibility form on the membrane surface because of the electro-osmosis process. This layer slows NO gas diffusion to the MoS_2 active sites and as NO has low solubility in water, the reaction undergoes to HER instead of NORR. Changing the gas diffusion layer to hydrophobic carbon paper improves the removal of the water layer formed during the reaction, promoting the desired NORR reaction over HER. Therefore, using carbon paper as a gas diffusion layer is the best combination for NORR. From the study of carbon ratio, product selectivity results also align with the previous RDE test results. Without a mixture of carbon, HER is the dominant reaction (81.0% FE towards H_2) with zero FE_{NH3}. HER reaction is suppressed by adding carbon black to the catalyst layer. FE_{NH3} increases to 60.0% with 40 wt.% carbon, while FE_{H2} drops to less than 12.7% at 2.1 V. The undesired HER is suppressed with an increasing carbon ratio, with 40MoS_2/60C showing the lowest FE (less than 10%) towards H_2.

Notably, pure MoS_2 with Ti GDL and carbon paper is more selective towards NH_2OH (**Figure S11(a &b)**). NH_2OH is a reaction intermediate towards NH_3 production via a NO reduction process and has high solubility in water.[43] Water contact angle measurements were performed to check the hydrophobicity of the as prepare catalyst layer on the membrane. Results are shown in **Figure 3(c)** and indicated that without additional carbon mixture, the contact angle of the catalyst layer is 125°, which is a bit more hydrophilic compared to that of adding extra carbon black (150° with 50 wt.% carbon black). Thus, we hypothesize that the water layer during the reaction or due to the electro-osmosis drag could not be removed efficiently, therefore the remaining water could potentially desorb NH_2OH from the active sites of MoS_2 and thus prevent further NH_3 formation. Carbon black can also improve the mass transport limitation of insoluble reactants which allows a dramatic reduction in the gas diffusion pathway, especially with low concentration NO. 50MoS_2/C displays the highest current density (78 mA·cm^{-2}) and FE towards NH_3 (86%

Journal of Materials Chemistry A Accepted Manuscript

This journal is © The Royal Society of Chemistry 20xx

Please do not adjust margins

View Article Online
DOI: 10.1039/D5TA00760J

at 2.1 V), which indicates not only more active site but also more reactant are available for the reaction.

The NH_3 production rate and partial current density results align with the previous results (**Figure 3(b)**). 50MoS_2/C achieves an excellent performance of 466 μmol·cm^{-2}·h^{-1}, while pure MoS_2 produces only 134 μmol·cm^{-2}·h^{-1} ammonia at 2.1 V. The NH_3 yield of other studied configurations is shown in **Figure S13** and a comparison table to the current literature is shown in Table S4. There is no NH_3 production using Ti GDL and the ammonia production rate reached a plateau at higher voltage which indicates the HER takes over than NORR. NH_3 partial current density follows the same trend as ammonia production rate for all measurements. The single pass NO conversion rate is summarized in **Figure S14**. A major advantage of conducting NORR in a PEM electrolyzer is that it is suitable for continuous NO conversion, which is beneficial for scaled-up operations often required in chemical industry. The enhanced performance by mixing with carbon black can be ascribed to the significant increase in the mass transport rate through hydrophobic carbon layer, which can further compensate for the low concentration NO gas inlet, thereby inhibiting excess *H for H_2 generation. However, with excess amount of carbon, the availability of active sides was hindered, and less catalytic activity was observed.

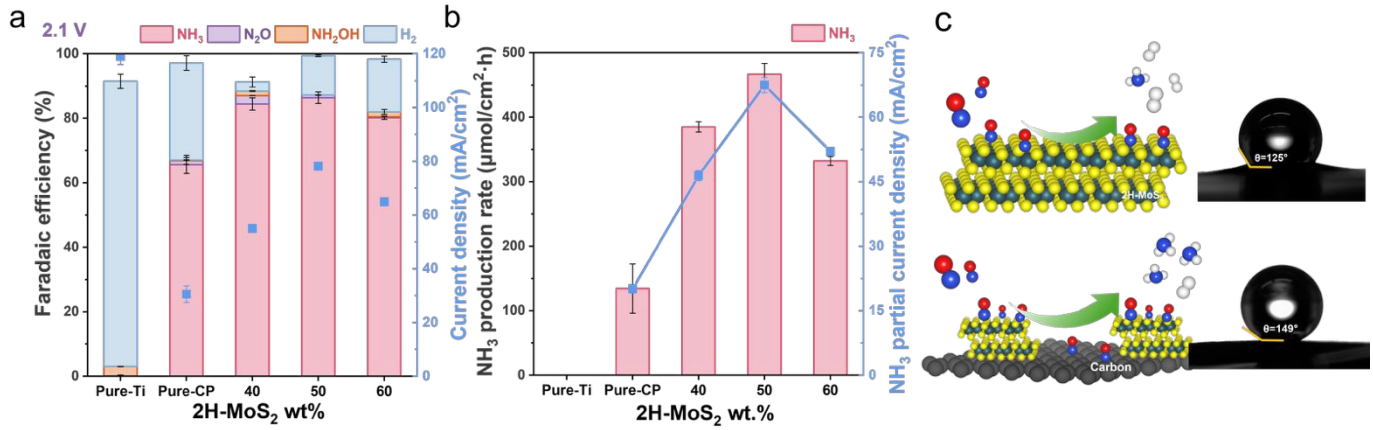

Figure 3. (a) Faradaic efficiency & total current density; (b) ammonia production rate & partial current density of 2H-MoS_2 at no or different degree of mixing with carbon black; (c) schematic illustrations and water-contact angle measurement of the enhanced NO mass transport.

According to previous findings, physical mixture with 50 wt.% carbon black was used to compare the catalytic performance of NORR between 2H- and 1T'-MoS_2. Electrochemical impedance spectroscopy (EIS) in **Figure 4(a)** reveals that the 1T' phase exhibits a significantly lower charge transfer resistance (R_{ct}) compared to the 2H phase. While R_{ct} primarily reflects the kinetic barrier for the reaction at the interface, this drastic reduction suggests that the semi-metallic character of the 1T' phase facilitates rapid electron transfer to surface active sites. Furthermore, the lower ohmic cell resistance (R_s) observed in the 1T' sample confirms the improved bulk electrical conductivity.

The reduction of NO to NH_4^+ is a 5-electron and 6-proton multistep reaction ($NO + 6H^+ + 5e^- \rightarrow NH_4^+ + H_2O$) and the N-N coupling is a critical step to detoxify NO to harmless dinitrogen. However, the NH_4^+ production in this reaction could compete with N-N coupling ($2NO + 4H^+ + 4e^- \rightarrow N_2 + 2H_2O$ & $2NO + 2H^+ + 2e^- \rightarrow N_2O + H_2O$). The faradaic efficiency and product selectivity of electrocatalytic NO reduction on 2H- and 1T'-MoS_2 at different cell potentials in PEM electrolyzer are shown in **Figure 4 (b & c)**. 2H-MoS_2 shows markedly higher selectivity toward ammonia than 1T'-MoS_2 over the entire cell-voltage range. As the cell voltage increases, FE_{NH3} increases and reaches a maximum of 86% at 2.1 V with current density of 78 mA·cm^{-2}. The ammonia production rate also increases with cell potential, although the rate of increase becomes smaller at higher voltages, indicating that the additional current is diverted to the competing HER rather than to NO reduction (**Figure S15(a)**). Consistently, at higher cell voltages FE_{NH3} decreases while FE_{H2} increases, confirming that HER becomes increasingly dominant.

In contrast, 1T'-MoS_2 shows a lower NH_3 selectivity, with FE_{NH3} maximum of 48% at 1.9 V. Notably, 1T'-MoS_2 shows displays substantially higher N_2 selectivity at low cell voltage, reaching around 50% FE_{N2} at 1.7 V, but this N_2 selectivity rapidly diminishes to <1% at 2.3 V. With increasing cell voltage, the product distribution on 1T' shifts away from N_2 toward NH_3 and ultimately toward H_2, suggesting that the higher driving force increasingly promotes proton-coupled processes and HER that suppress NORR. This is further supported by the decline in NH_3 production rate and the decrease in NH_3 partial current density at the highest voltages, despite the increase in total current, highlighting that the additional current is largely consumed by HER (**Figure S15(b)**).

The single pass NO conversion rate of 2H- and 1T'-MoS_2 is presented in **Figure S15(c)**, 2H-MoS_2 exhibits higher NO conversion than 1T'-MoS_2, reaches around 67% at 2.3 V which is 3.4 times higher than that of 1T'-MoS_2. One way to assess the accessibility of active sites in both catalysts is by comparing the pore size distribution of these materials. Thus, the specific surface area and porosity of the as-prepared 2H- and 1T'-MoS_2 were characterized via N_2 adsorption-desorption isotherms

Open Access Article. Published on 14 April 2026. Downloaded on 21/4/2026 3:58:20 PM.
This article is licensed under a Creative Commons Attribution 3.0 Unported Licence.

Journal of Materials Chemistry A Accepted Manuscript

Please do not adjust margins

View Article Online
DOI: 10.1039/D5TA09769J

(**Figures S16**). For 2H- and 1T'-MoS_2, the major pores size is centred at 4 nm, while 2H-MoS_2 shows few smaller and larger size distribution compared to 1T'-MoS_2. 2H-MoS_2 exhibited a specific surface area (SSA) of 33 $m^2 \cdot g^{-1}$, which is approximately 3 times greater than that of the 1T'-MoS_2 (13 $m^2 \cdot g^{-1}$). The lower SSA of the 1T' phase reflects this dense spherical aggregation, which limits the access of gas to the internal surfaces compared to the more open 2H morphology (**Figure 1 (b &c)**).Based on the above results, it implies that under electrocatalytic conditions, 2H-MoS_2 could offer more accessibility to the reactant NO, which is beneficial especially in low concentration NO feed.

Our experimental results show that two different phases of MoS_2 display markedly different NORR selectivity, with 1T' favoring N_2 formation and 2H favoring NH_3 formation. To rationalize this difference, we have performed kinetics study and ex situ Diffuse reflectance infrared Fourier transform spectroscopy (DRIFTS) measurements. As shown in **Figure 4 (d &e)**, 2H-MoS_2 does not show a clear growth of distinct NO-related adsorption bands and is dominated by water signal, whereas 1T'-MoS_2 displays pronounced NO adsorption peak. The intensity of the signal at 1683 cm^{-1}, which corresponds to the coupled mononitrosyl or dinitrosyl adsorption[44], increased substantially. This results also indicate that 1T' phase has high surface coverage of NO compared to that of 2H phase, which can promote the N-N coupling.

To compare kinetics on a consistent basis, we evaluate the local Tafel/derivative behavior and the apparent NORR kinetic isotope effect (apparent KIE)[45] within the same potential window (-0.262 V to -0.296 V vs. RHE). The decision of the potential is shown in **Figure S17**. 2H exhibits a flatter and more stable d(log|j|)/dE response, whereas 1T' shows a much steeper (more potential-sensitive) derivative, indicating different apparent rate-control characteristics. Importantly, the isotope response in the same window reveals a pronounced apparent KIE for 2H (~1.85) but an approximately unity KIE for 1T' (**Figure S18**). The strong isotope sensitivity on 2H suggests that proton-involving sub-steps contribute substantially to the overall rate in this regime,[46] consistent with enhanced NH_3 selectivity, while the near-unity KIE on 1T' indicates that the dominant current-determining step is comparatively H/D-insensitive.

Taken together, 1T' stabilizes NO-derived adsorbates more strongly, enabling higher NO* coverage and facilitating N-N coupling routes toward N_2, while 2H proceeds via more proton-coupled hydrogenation pathway that correlates with enhanced NH_3 selectivity.[47]

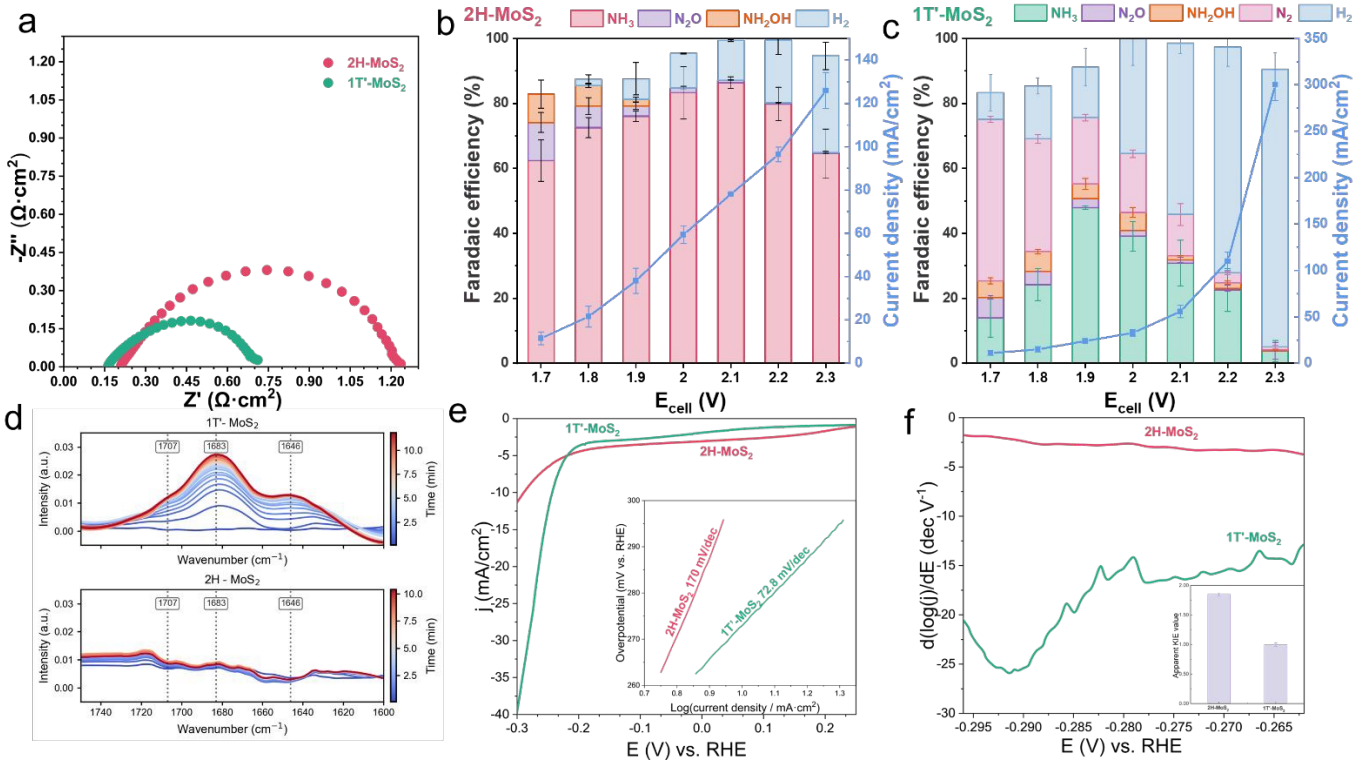

Figure 4. (a) EIS measurement for 2H and 1T' MoS_2; (b & c) faradaic efficiency and total current density for 2H and 1T' phase MoS_2; (d) NO adsorption for 2H and 1T' phase MoS_2; (e) LSV and Tafel slop; (f) local Tafel derivative and apparent KIE values for 2H and 1T' phase MoS_2.

The metallic phase 1T'-MoS_2 is known to be metastable with higher ground-state energy than the semiconducting 2H-MoS_2. Consequently, it can undergo phase transformation to the 2H structure during reactions.[48, 49] *Ex situ* XPS is performed to clarify the stability of both 2H- and 1T'-MoS_2 after the NORR (**Figure 5 (a-d)**). For 1T'-MoS_2, the XPS results indicate a

This journal is © The Royal Society of Chemistry 20xx

Please do not adjust margins

Open Access Article. Published on 14 April 2026. Downloaded on 21/4/2026 3:58:20 PM.
This article is licensed under a Creative Commons Attribution 3.0 Unported Licence.

Journal of Materials Chemistry A Accepted Manuscript

View Article Online
DOI: 10.1039/D5TA09760J

Open Access Article. Published on 14 April 2026. Downloaded on 21/4/2026 3:58:20 PM.
This article is licensed under a Creative Commons Attribution 3.0 Unported Licence.

Journal of Materials Chemistry A Accepted Manuscript

reduction in the 1T' phase after the reaction, accompanied by a pronounced increase in the 2H phase and Mo (V)/Mo (VI) species. This suggests the transformation of unstable Mo species into more thermodynamically stable forms. In comparison, 2H-MoS_2 exhibits similar changes in the Mo 3d spectra but with greater structural stability following the reaction. The relative atomic ratio of different Mo species is shown in **Table S3**. The results reveal a significant increase in Mo(V) and Mo(VI) compounds in 1T'-MoS_2-from 5% to 56% after reaction. This substantial increase implies that more Mo(V) species were formed during the reaction, which were subsequently oxidized to Mo(VI), likely due to exposure to NO, air, or H_2O.[50, 51] These findings corroborate the enhanced formation of N-N coupling products observed for 1T'-MoS_2, highlighting Mo(V) as a key intermediate in the reaction pathway. Notably, the S 2p spectra show an additional spin–orbit doublet (at 163.6 and 164.8 eV) in both MoS_2 phases after the reaction, relative to their fresh counterparts. This signal is attributed to $(S_2)^{2-}$ species, commonly found in amorphous sulfur-rich MoS_3, indicating the possible formation of $MoOS_2$ during the reaction process.[52-54] The 1T'-MoS_2 sample shows a higher abundance of $(S_2)^{2-}$ species compared to 2H-MoS_2, which is consistent with the corresponding Mo 3d spectra. These bridging disulfide species $(S_2)^{2-}$) serve as active protonation sites, potentially enhancing the hydrogen evolution reaction (HER), particularly under higher applied voltages.[55, 56]

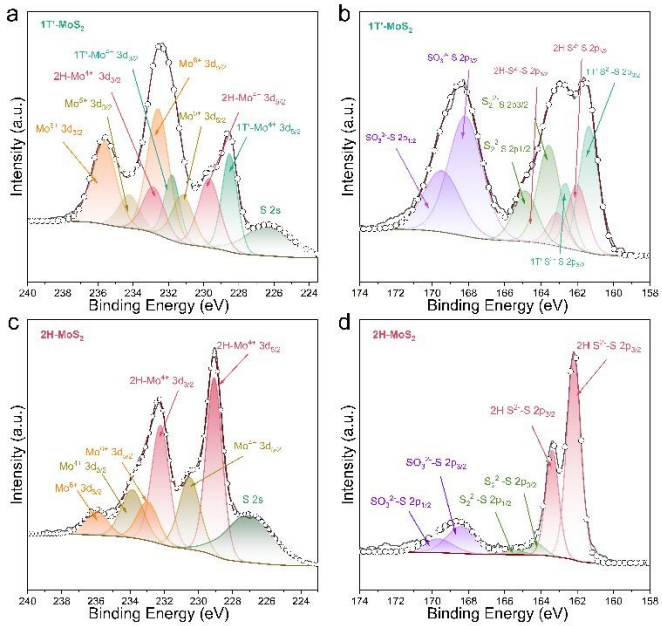

Figure 5. (a & c) Mo 3*d* XPS spectra; (b & d) S 2*p* XPS spectra of 2H and 1T' phase MoS_2 after reaction.

Conclusion

In conclusion, our study explores 2H and 1T' phases of MoS_2 and their effects on activity and selectivity towards multi-step proton-electron transfer electrocatalytic NO reduction. Through different carbon mixture experiments and testing different gas diffusion layer materials, we identified that the hydrophobicity of the catalyst layer enhances the adsorption of NO and improved the NO coverage on the catalyst surface, thus promoting NO reduction especially in low NO concentration steam. The optimal physically carbon mixture ratio of 50 wt.% led to high FE towards NH_3 and low HER reaction rate. By regulating different crystal phases of MoS_2 (2H and 1T'), the selectivity of products significantly changed from NH_3 to N_2. 2H exhibits a large apparent KIE (~1.85) while 1T' remains near unit, together with distinct local Tafel/derivative signatures, indicating fundamentally different apparent rate-control characteristics and a stronger proton-coupled contribution on 2H. Additionally, for 2H-MoS_2, 67% of single-pass NO conversion rate and 558 $\mu mol \cdot cm^{-2} \cdot h^{-1}$ ammonia production rate was achieved at 2.3 V. Our investigation showed that electrocatalytic selectivity of MoS_2 or other transition metal dichalcogenides can be markedly regulated by phase engineering, utilizing the sequential proton-electron transfer pathways could change the selectivity of complex multistep reactions. Our work could inspire future NORR electrocatalysts design, which could be further expanded to other complex multistep reactions like electrochemical CO/CO_2 reduction.

Experimental section

Chemicals and Materials

Thiourea ($SC(NH_2)_2$), Ammonium hepta-molybdate tetrahydrate ($(NH_4)_6Mo_7O_{24} \cdot 4H_2O$), hydrazine monohydrate ($N_2H_4 \cdot H_2O$), Hydrogen peroxide (H_2O_2), Sulfuric acid (H_2SO_4), Potassium iodate (KIO_3), hydrolymine (NH_2OH) and neutral red were purchased from Sigma Aldrich. Iridium (IV) oxide Premion™ (IrO_2) 99.99% was purchased from Therma Scientific Chemicals. Vulcan XC72 carbon black was bought from Cabot Corporation. Nafion™ 115 membranes from Ion power, porous sintered titanium gas diffusion layers were purchased from Bekaert, and carbon gas diffusion layer (GDL) Sigracet 39 BB was from Fuel Cell Store.

Preparation of 2H-MoS_2 nanosheets

2H-MoS_2 was synthesized using hydrothermal method. Briftly, 0.53 g (0.4 mmol) of $(NH_4)_6Mo_7O_{24} \cdot 4H_2O$ and 1.83 g (24 mmol) of $SC(NH_2)_2$ were dissolved in 30 mL of MilliQ water and stirred to form a homogeneous solution. After that, the solution was transferred to a 45 mL stainless-steel autoclave with Polyparaphenol (PPL) liner and heated to 220 °C for 12 hours. After cooling down naturally to room temperature, the products were extracted, filtered and washed with water and ethanol for 6 times. The obtained catalyst powder was dried the vacuum oven at 60 °C for 12 hours.

Preparation of 1T'-MoS_2 nanosheets

1T' phase dominated MoS_2 was synthesized by one-step hydrazine assisted hydrothermal method which is modified by as described 2H-MoS_2 method previously. Additionally, 0.29 mL (6 mmol) of $N_2H_4 \cdot H_2O$ with the molar ratio of N_2H_4/Mo of 2:1 was added into the solution. The synthesis was completed in 180 °C for 10 hours and rapidly

View Article Online
DOI: 10.1039/D5TA09769J

cooled down to room temperature. The rest remained the same as the synthesis of 2H-MoS_2 samples.

Materials characterization

The powder X-ray diffraction (XRD) was recorded using Bruker D8 ADVANCE X-ray diffractometer with Cu Kα radiation source in a range of 5° to 90° with a step of 0.05°. The surface morphology of the catalysts was characterized by scanning electron microscopy (SEM). Raman spectra were recorded from 500 to 3000 cm^{-1} on a Horiba Scientific LabRAM HR Evolution Raman Spectroscopy system with an excitation wavelength of 514 nm. The composition and chemical bonding were analyzed by Thermo Scientific Kα system with Al Kα radiation (1486.7 eV). All binding energies for XPS spectra were calibrated according to the C 1s peak at 284.8 eV. Contact angle measurements were performed via sessile drop using an OCA 25 goniometer (Dataphysics instruments Gmbh, Filderstadt, Germany), and 2 µL of droplets were dispensed onto substrates using an automatic pipetting unit. Measurements were taken in ambient air with a temperature in the range of 20–24 °C. Specific surface areas were determined by the Brunauer-Emmett-Teller (BET) method. The Mo K-edge X-ray absorption near-edge (XANES) spectra and X-ray absorption fine structure (EXAFS) spectra were measured at the BL16-NOTOS beamline of the ALBA Synchrotron, Spain.

Electrode preparation

Nafion™ 115 membranes (3×3 cm^2) were pre-treated according to the procedure of 1 hour in 5 wt. % hydrogen peroxide (H_2O_2) solution and 1 hour in 0.5 M H_2SO_4 solution at 80°C and 1 hour in boiling MilliQ water. 4 mg of commercial IrO_2 (1 mg·cm^{-2}) with 20 wt.% Nafion ionomers were ultrasonically dispersed in 1mL isopropanol and water (volume ratio: 50:50) for 1 hour to get a homogenous ink. The cathodic ink was prepared in the same way with as prepared 2H-MoS_2 or 1T'-MoS_2, Vulcan XC72 carbon black (from 10 wt.% to 70 wt.%) and 30 wt.% Nafion ionomers to get a constant catalyst loading of 1 mg·cm^{-2} 2H-MoS_2 or 1T-MoS_2 with a 2×2 cm^2 active geometry area. The catalyst inks were finally sprayed at 60 °C onto both side of membranes using automatic spray coater (CNC Airbrush Singular). After spray coating, the membrane was hot-pressed at 120 °C and 1 tonne for 3 minutes.

Electrochemical NO reduction test

The electrochemical NO reduction experiments were conducted in the PEM electrolyser (**Figure S19**) on an AUTOLAB PGSTAT302N potentiostat equipped with a 20 A booster. The PEM electrolyser was operating at 80°C. For electrochemical NO reduction, at the cathode chamber, the mixture of 5% NO and 4% CH_4 in He flowed at 27 mL·min^{-1}. CH_4 was acting as the internal standard to correct the volume changes during reactions. at the anode chamber, MilliQ water was supplied at the flow rate of 1 mL·min-1 by a peristaltic pump (Ismatec). After the reaction, the cathode chamber outlet was connected to an acid trap with 0.1 M H_2SO_4 solution to trap the produced ammonia (NH_3) and hydrolymine (NH_2OH). After the acid trap, the gas flowed to the connected Bruker ALPHA infrared spectrometer and gas chromatography (GC). The reactions were carried out at constant potential in the range of 1.7 V to 2.3 V for 30 minutes each. Electrochemical impedance spectroscopy (EIS) was conducted at the catalytically relevant potential of 1.7 V over a frequency range of 100 kHz to 0.1 Hz, using 10 points per decade and an AC perturbation amplitude of 10 mV.

Production quantification

The gaseous NO reduction products nitrous oxide (N_2O) and unreacted NO, external standard CH_4 were analysed by Bruker Alpha infrared spectrometer. N_2 and H_2 were analysed by a CompactGC (Global Analyser Solutions) equipped with a thermal conductivity detector (TCD). Ammonium (NH_4^+) collected at the acid trap were quantified using Ion Chromatography (IC, Metrohm 883 Basic ion chromatography), equipped with a Metrosep C6 separation column. Hydroxylamine (NH_2OH) was quantified by UV–Vis spectroscopy (Unicam UV 500), measuring absorbance at 525 nm. The procedure consists in adding 1 mL of the sample with 5 mL of MilliQ water, 1 mL of 0.047 mol·L^{-1} KIO_3 and 1 mL of 3M H_2SO_4, 2 mL of neutral red is added after 5 minutes. The calibration curve of the natural red method for quantifying NH_2OH is shown in **Figure S20**.

RDE measurements

Cyclic voltammetry (CV) and linear scan voltammetry (LSV) were conducted using a three-electrode electrochemical glass cell (graphene rod as counter and Ag/AgCl as reference electrodes) at room temperature with Argon and NO purging. A glassy carbon disc of 0.196 cm^2 (5 mm diameter) was used as the working electrode in rotating disk electrode measurements (RDE, Pine Instruments). 15 µL of catalyst ink (details described in the previous section) was loaded onto the glassy carbon electrode for all the measurements in 100 mL of freshly prepared 0.1 M H_2SO_4 solution. Prior to the measurements, the electrode as electrochemically cleaned by repetitive potential scans between -0.4 V to 0.8 V vs. RHE until a stable cyclic voltammogram was obtained. All potentials were converted into the reversible hydrogen electrode (RHE) scale, and 85% iR corrections were applied to all results. Apparent NORR kinetic isotope effect was measured in a batch type H-cell in 0.1 M H_2SO_4 electrolyte and 0.1 M D_2SO_4 with NO saturation. The pH

Data availability

The data generated and analysed in this study are included in the article and its Supplementary Information (SI). Supplementary information: further characterization data of as synthesized MoS_2 catalysts (XPS, EXAFS fitting data, BET), electrochemical test data.

Acknowledgements

M.L. acknowledge funding from China Scholarship Council. Authors are grateful to ALBA synchrotron for beamtime at NOTOS beamline (proposal number: 2024098746).

Author contributions

M.L. and A.U. conceived the project. M.L. led experiments, data analysis, and figure design. F.H.B. assisted with electrochemical testing and scientific discussion. B.L. assisted with Raman measurement. M.C. assisted with electrochemical testing in RDE set-up. S.M. assisted with X-ray absorption measurement. R.K. assisted

Open Access Article. Published on 14 April 2026. Downloaded on 21/4/2026 3:58:20 PM.
This article is licensed under a Creative Commons Attribution 3.0 Unported Licence.

Journal of Materials Chemistry A Accepted Manuscript

This journal is © The Royal Society of Chemistry 20xx

Please do not adjust margins

with scientific discussion. A.U. assisted with project supervision and scientific discussion. M.L. and A.U. wrote the manuscript with editing contributions from all the authors.

Competing interests

The authors declare no competing interests.

References

1. J. I. Sprent, *The ecology of the nitrogen cycle*, Cambridge University Press, 1987.
2. V. Rosca, M. Duca, M. T. de Groot and M. T. M. Koper, *Chemical Reviews*, 2009, **109**, 2209-2244.
3. J. Leverett, W. H. Lie, M. H. A. Khan, Z. Ma, R. Daiyan and R. Amal, *Sustainable Energy & Fuels*, 2025, **9**, 3780-3790.
4. L. Alves, L. I. V. Holz, C. Fernandes, P. Ribeirinha, D. Mendes, D. P. Fagg and A. Mendes, *Renewable and Sustainable Energy Reviews*, 2022, **155**, 111916.
5. M. Okubo and T. Kuwahara, in *New Technologies for Emission Control in Marine Diesel Engines*, eds. M. Okubo and T. Kuwahara, Butterworth-Heinemann, 2020, pp. 53-143.
6. V. Praveena and M. L. J. Martin, *Journal of the Energy Institute*, 2018, **91**, 704-720.
7. M. Pinzón, R. García-Carpintero, A. R. de la Osa, A. Romero, D. Abad-Correa and P. Sánchez, *Energy Conversion and Management*, 2024, **321**, 118998.
8. M. Van Damme, L. Clarisse, S. Whitburn, J. Hadji-Lazaro, D. Hurtmans, C. Clerbaux and P.-F. Coheur, *Nature*, 2018, **564**, 99-103.
9. J. Humphreys, R. Lan and S. Tao, *Advanced Energy and Sustainability Research*, 2021, **2**, 2000043.
10. J. Long, S. Chen, Y. Zhang, C. Guo, X. Fu, D. Deng and J. Xiao, *Angewandte Chemie International Edition*, 2020, **59**, 9711-9718.
11. Y.-w. Wu, H.-w. Wang, Z.-l. Wu, X. Zhang, Y. Dong, Z. Hu, Y. Lv, X.-y. Zhou, L. Zhao, B. Zhang and Q. Lu, *Separation and Purification Technology*, 2025, **366**, 132813.
12. J. H. Montoya, C. Tsai, A. Vojvodic and J. K. Nørskov, *ChemSusChem*, 2015, **8**, 2180-2186.
13. B. H. Ko, B. Hasa, H. Shin, Y. Zhao and F. Jiao, *Journal of the American Chemical Society*, 2022, **144**, 1258-1266.
14. H. Wan, A. Bagger and J. Rossmeisl, *Angewandte Chemie International Edition*, 2021, **60**, 21966-21972.
15. R. Sander, *Atmos. Chem. Phys.*, 2023, **23**, 10901-12440.
16. S. Bunea, M. Coppens and A. Urakawa, *ACS Catalysis*, 2023, **13**, 11345-11351.
17. M. Li, J. Verkuil, S. Bunea, R. Kortlever and A. Urakawa, *ChemSusChem*, 2023, **16**, e202300949.
18. W. Yang, H. Liu, X. Chang, Y. Zhang, Y. Cai, Y. Li, Y. Cui, B. Xu, L. Yu, X. Cui and D. Deng, *Nature Communications*, 2025, **16**, 1257.
19. A. C. A. de Vooys, M. T. M. Koper, R. A. van Santen and J. A. R. van Veen, *Electrochimica Acta*, 2001, **46**, 923-930.
20. Z. Wang, H. Duan, W. Qu, H. Zhang, L. Han, Z. Teng, G. Chen, D. Cheng, X. Wang, Y. A. Wu, M. Xie and D. Zhang, *Advanced Functional Materials*, 2025, **35**, 2507533.
21. J. Meng, C. Cheng, Y. Wang, Y. Yu and B. Zhang, *Journal of the American Chemical Society*, 2024, **146**, 10044-10051.
22. H. Chen, Y. Gao, J. Du, R. Hao, X. Wu, L. Wang and Z. Wu, *ACS Nano*, 2026, **20**, 2323-2336. View Article Online DOI: 10.1039/D5TA09769J
23. J. Theerthagiri, K. Karuppasamy, A. H. Mahadi, C. J. Moon, N. Rahamathulla, S. Kheawhom, S. Alameri, A. Alfantazi, A. P. Murthy and M. Y. Choi, *Environmental Chemistry Letters*, 2024, **22**, 189-208.
24. A. Mukherjee, N. Ojha, K. K. Pant, A. Deb, M. Abdinejad, S. S. Mahapatra and B. C. Ruidas, *Environmental Science & Technology Letters*, 2025, **12**, 1113-1138.
25. W. Zhai, Z. Li, Y. Wang, L. Zhai, Y. Yao, S. Li, L. Wang, H. Yang, B. Chi, J. Liang, Z. Shi, Y. Ge, Z. Lai, Q. Yun, A. Zhang, Z. Wu, Q. He, B. Chen, Z. Huang and H. Zhang, *Chemical Reviews*, 2024, **124**, 4479-4539.
26. Y. Liu, M. Tursun, G. Hu, A. Abdukayum and C. Wu, *RSC Advances*, 2025, **15**, 29323-29334.
27. D. He, H. Ooka, Y. Kim, Y. Li, F. Jin, S. H. Kim and R. Nakamura, *Proceedings of the National Academy of Sciences*, 2020, **117**, 31631-31638.
28. Y. Wang, Y. Xu, C. Cheng, B. Zhang, B. Zhang and Y. Yu, *Angewandte Chemie*, 2024, **136**, e202315109.
29. M. Li, Z. Zhou, L. Hu, S. Wang, Y. Zhou, R. Zhu, X. Chu, A. Vinu, T. Wan, C. Cazorla, J. Yi and D. Chu, *ACS Applied Materials & Interfaces*, 2022, **14**, 16338-16347.
30. M. Acerce, D. Voiry and M. Chhowalla, *Nature Nanotechnology*, 2015, **10**, 313-318.
31. J. Zheng, H. Zhang, S. Dong, Y. Liu, C. Tai Nai, H. Suk Shin, H. Young Jeong, B. Liu and K. Ping Loh, *Nature Communications*, 2014, **5**, 2995.
32. M. Li, D. Wang, J. Li, Z. Pan, H. Ma, Y. Jiang and Z. Tian, *RSC Advances*, 2016, **6**, 71534-71542.
33. K. Wu, X. Cao, M. Li, B. Lei, J. Zhan and M. Wu, *Small*, 2020, **16**, 2006532.
34. J. Xie, H. Zhang, S. Li, R. Wang, X. Sun, M. Zhou, J. Zhou, X. W. Lou and Y. Xie, *Advanced Materials*, 2013, **25**, 5807-5813.
35. X. Fan, P. Xu, D. Zhou, Y. Sun, Y. C. Li, M. A. T. Nguyen, M. Terrones and T. E. Mallouk, *Nano Letters*, 2015, **15**, 5956-5960.
36. L. Cai, J. He, Q. Liu, T. Yao, L. Chen, W. Yan, F. Hu, Y. Jiang, Y. Zhao, T. Hu, Z. Sun and S. Wei, *Journal of the American Chemical Society*, 2015, **137**, 2622-2627.
37. Z. Liu, J. Ou, H. Wang, X. You and M. Ye, *ACS Applied Materials & Interfaces*, 2016, **8**, 32060-32067.
38. L. Feng, L. Zhang, S. Zhang, X. Chen, P. Li, Y. Gao, S. Xie, A. Zhang and H. Wang, *ACS Applied Materials & Interfaces*, 2020, **12**, 17547-17556.
39. A. Azcatl, X. Qin, A. Prakash, C. Zhang, L. Cheng, Q. Wang, N. Lu, M. J. Kim, J. Kim, K. Cho, R. Addou, C. L. Hinkle, J. Appenzeller and R. M. Wallace, *Nano Letters*, 2016, **16**, 5437-5443.
40. Q. Liu, X. Li, Q. He, A. Khalil, D. Liu, T. Xiang, X. Wu and L. Song, *Small*, 2015, **11**, 5556-5564.
41. H. Husain, M. Sulthonul, B. Hariyanto, C. Cholsuk and S. Pratapa, *Materials Today: Proceedings*, 2021, **44**, 3296-3300.
42. S. Nösberger, J. Du, J. Quinson, E. Berner, A. Zana, G. K. H. Wiberg and M. Arenz, *Electrochemical Science Advances*, 2023, **3**, e2100190.
43. S. Garcia-Segura, M. Lanzarini-Lopes, K. Hristovski and P. Westerhoff, *Applied Catalysis B: Environmental*, 2018, **236**, 546-568.

Open Access Article. Published on 14 April 2026. Downloaded on 21/4/2026 3:58:20 PM. This article is licensed under a Creative Commons Attribution 3.0 Unported Licence.

Journal of Materials Chemistry A Accepted Manuscript

Please do not adjust margins

View Article Online
DOI: 10.1039/D5TA09769J

44. L. van Haandel, E. J. M. Hensen and T. Weber, *Catalysis Today*, 2017, **292**, 67-73.
45. X. Gao, X.-Y. Yu and C.-R. Chang, *Physical Chemistry Chemical Physics*, 2022, **24**, 15182-15194.
46. S. Hammes-Schiffer, *Accounts of Chemical Research*, 2025, **58**, 1335-1344.
47. D. He, H. Ooka, Y. Li, Y. Kim, A. Yamaguchi, K. Adachi, D. Hashizume, N. Yoshida, S. Toyoda, S. H. Kim and R. Nakamura, *Nature Catalysis*, 2022, **5**, 798-806.
48. K.-A. N. Duerloo, Y. Li and E. J. Reed, *Nature Communications*, 2014, **5**, 4214.
49. J. Heising and M. G. Kanatzidis, *Journal of the American Chemical Society*, 1999, **121**, 638-643.
50. X. Zhang, F. Jia, B. Yang and S. Song, *The Journal of Physical Chemistry C*, 2017, **121**, 9938-9943.
51. H. Li, S. Chen, Y. Zhang, Q. Zhang, X. Jia, Q. Zhang, L. Gu, X. Sun, L. Song and X. Wang, *Nature Communications*, 2018, **9**, 2452.
52. L. Benoist, D. Gonbeau, G. Pfister-Guillouzo, E. Schmidt, G. Meunier and A. Levasseur, *Thin Solid Films*, 1995, **258**, 110-114.
53. J. C. Dupin, D. Gonbeau, I. Martin-Litas, P. Vinatier and A. Levasseur, *Applied Surface Science*, 2001, **173**, 140-150.
54. D. Ryaboshapka and P. Afanasiev, *Journal of Catalysis*, 2023, **426**, 30-38.
55. P. D. Tran, Thu V. Tran, M. Orio, S. Torelli, Q. D. Truong, K. Nayuki, Y. Sasaki, Sing Y. Chiam, R. Yi, I. Honma, J. Barber and V. Artero, *Nature Materials*, 2016, **15**, 640-646.
56. K. T. Santos, L. A. Z. Sanchez, V. Martin, F. Guillet, K. Kumar, X. Portier, F. Maillard, L. Oliviero and L. Dubau, *Electrochimica Acta*, 2024, **507**, 145195.

Open Access Article. Published on 14 April 2026. Downloaded on 21/4/2026 3:58:20 PM.
This article is licensed under a Creative Commons Attribution 3.0 Unported Licence.

Journal of Materials Chemistry A Accepted Manuscript

This journal is © The Royal Society of Chemistry 20xx

Please do not adjust margins

View Article Online
DOI: 10.1039/D5TA09769J

Data availability statements

The data supporting this article have been included as part of the Supplementary Information.

The authors will upload the figure data on a repository once they are finalised.

Open Access Article. Published on 14 April 2026. Downloaded on 21/4/2026 3:58:20 PM.
This article is licensed under a Creative Commons Attribution 3.0 Unported Licence.

Journal of Materials Chemistry A Accepted Manuscript